Solar Energy Materials & Solar Cells 251 (2023) 112169

Contents lists available at ScienceDirect

Solar Energy Materials and Solar Cells

journal homepage: www.elsevier.com/locate/solmat

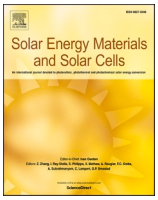

Effects of ITO based back contacts on Cu(In,Ga)Se_2 thin films, solar cells, and mini-modules relevant for semi-transparent building integrated photovoltaics

Torsten Hölscher [a,*], Marcel Placidi [b,c,d], Ignacio Becerril-Romero [b], Robert Fonoll-Rubio [b], Victor Izquierdo-Roca [b], Angélica Thomere [b], Eduard Bailo [e], Thomas Schneider [a], Heiko Kempa [a,**], Roland Scheer [a], Alejandro Pérez-Rodríguez [b,f]

[a] Martin-Luther-University Halle-Wittenberg, Institute of Physics, Photovoltaics Group, 06120, Halle, Germany
[b] Institut de Recerca en Energia de Catalunya (IREC), Materials Avancats per a l'Energia, Jardins de les Dones de Negre 1, 2a Planta, 08930, Sant Adrià de Besòs, Barcelona, Spain
[c] Universitat Politècnica de Catalunya (UPC), Photovoltaic Lab – Micro and Nano Technologies Group (MNT), Electronic Engineering Department, EEBE, Av. Eduard Maristany 10-14, 08019, Barcelona, Spain
[d] Universitat Politècnica de Catalunya (UPC), Barcelona Center for Multiscale Science & Engineering, Av. Eduard Maristany 10-14, 08019, Barcelona, Spain
[e] Francisco Albero S.A.U. (FAE), C. Rafael Barrades, 19, 08908, L'Hospitalet de Llobregat, Spain
[f] IN2UB, Departament d'Enginyeria Electrònica i Biomèdica, Universitat de Barcelona, Carrer de Martí i Franquès 1, 08028, Barcelona, Spain

A B S T R A C T

This study presents the results of the development of semi-transparent Cu(In,Ga)Se_2 (CIGSe) mini-modules for the application in building integrated photovoltaics (BIPV). Applying in-situ X-ray diffraction in real-time during CIGSe growth we find that the bulk of indium-tin-oxide (ITO), acting as the transparent back contact, is chemically stable in CIGSe processing. CIGSe layers grown on reactively sputtered ITO (Ar/O_2 flux ratio = 60:1) or on ITO annealed in ambient air have a proportionally higher (220/204) orientation compared to CIGSe layers grown on as fabricated ITO sputtered solely by Ar. However, independent from the fabrication and annealing state of the ITO back contact, after CIGSe deposition at high substrate temperatures ≥600 °C accumulation of Ga at the CIGSe/ITO back contact interface combined with reduced solar cell efficiency is observed. This Ga accumulation visible in elemental depth profiles is attributed to the formation of gallium-oxide (GaO_x). Applying a very thin (≈10–30 nm) functional molybdenum layer in between CIGSe and the ITO back contact inhibits the formation of GaO_x. Based on this Mo/ITO back contact configuration semi-transparent 10 × 10 cm^2 mini-modules with 14 cells interconnected in series have been fabricated. Module parameters resulted in a fill factor of 63% and >12% in efficiency. The solar active coverage of the modules amounts to ≈70%, and the average visible transmittance (in the range 380–780 nm) of the transparent sections was 27.6% (9.6% for the total area of the device). Optimisation of the Mo/ITO contact allows increasing this transparency to values > 50%. Long-term outdoor testing of a semi-transparent module prototype reveals no degradation in electric output power for 3 months, demonstrating the device stability under changing climatic conditions.

1. Introduction

In the last decades, photovoltaic systems based on the Cu(In,Ga)Se_2 (CIGSe) thin film technology have demonstrated long term stability combined with high conversion efficiencies at low manufacturing costs [1–3]. Next to flexible solar cells, the application of CIGSe in building integrated photovoltaics (BIPV) is promising due to the possibility of glass facade elements coated with PV modules [4]. For window applications, semi-transparent solar cells are essential for providing electrical energy together with light and heat management [5].

In the case of CIGSe solar cells, semi-transparency can be straightforward achieved by (1) the growth of thinner absorber layers with a thickness (<500 nm) below the absorption length of the spectral range of interest [6,7]. Another method is (2) the local deposition [8] or local removal of opaque solar cell regions, generating complementary regions of complete optical transparency [9]. Advantages of (1) over (2) are the elimination of additional process steps like the selective removal as well as less material consumption combined with reduced deposition times [10]. Method (2), however, allows a simple adjustment of module transparency through the ratio of transparent and opaque areas.

* Corresponding author.
** Corresponding author.
E-mail addresses: torsten.hoelscher@physik.uni-halle.de (T. Hölscher), heiko.kempa@physik.uni-halle.de (H. Kempa).

https://doi.org/10.1016/j.solmat.2022.112169
Received 26 October 2022; Received in revised form 19 December 2022; Accepted 20 December 2022
Available online 22 December 2022

Furthermore, method (2) allows employing thicker CIGSe absorbers. From the electrical point of view, thicker absorbers make the device less sensitive to back contact (BC) recombination and reduce the shunt problem [10–13]. With regard to the monolithic interconnection, a thicker CIGSe absorber results in a higher reliability of the functionality of the final module in view of the side wall coverage of the P1 trench with $d_{CIGSe} > d_{BC}$ where d_{BC} is the thickness of the back contact layer. To the best of our knowledge, up to now no successful monolithic interconnection or even modules have been reported with an ultra-thin absorber layer.

This study focuses on demonstrating the feasibility of semi-transparent CIGSe modules by making use of the selective removal method. However, due to a back mirror effect of the Mo/glass substrates [14] the common Mo back contact for aesthetic aspects was replaced by tin-doped indium oxide In_2O_3:Sn (ITO). Generally, ITO shows a high electrical conductivity in combination with a high optical transparency in the visual spectral range, making this material suitable as a front as well as a back electrode in semi-transparent, bi-facial, and ultra-thin CIGSe solar cells [7,15–20]. In organic light emitting diodes (OLED) ITO has been proven as the standard hole injector for the organic p-type material [21,22]. Nakada et al. [23] first demonstrated the application of a transparent back contact based on ITO in CIGSe solar cells, reaching efficiencies on the same level and even beyond of those solar cells equipped with a standard Mo back contact. As shown by Schneider et al. in Ref. [16], the n^+-ITO/p-CIGSe junction exhibits an ohmic behaviour if the deposition of the CIGSe absorber was executed with a nominal substrate temperature of 480 °C (measured on the glass backside) [16]. However, at elevated substrate temperatures (≥520–550 °C), Nakada et al. [15] observed a deterioration of the J-V characteristics for solar cells with ITO back contacts, in particular the presence of a roll-over in the jV curve. This solar cell deterioration is often accompanied by the formation of gallium oxide (GaO_x) at the rear ITO/CIGSe interface. Noticeably, in the case of the front interface, efficient solar cells have been reported after introducing a GaO_x passivation layer in between the CIGSe and the CdS buffer layer [24] as well as after the complete substitution of the CdS buffer by a GaO_x layer [25,26]. Experiments of Heinemann et al. [25] revealed that alloying the GaO_x buffer with InO_x – giving $(Ga_y,In_{1-y})O_x$ – enhances recombination at the CIGSe/$(Ga_y,In_{1-y})O_x$ front interface with decreasing y. Whether this results from an increasing density of recombination active interface states or from an increasing electron affinity of $(Ga_y,In_{1-y})O_x$ with decreasing y or even both, is still an open question. However, applying the latter finding to the GaO_x formation at the ITO/CIGSe rear interface, then with increasing y a diminishing hole transport over the ITO/$(Ga_y,In_{1-y})O_x$/CIGSe interface should be observed. Hence, a Ga rich $(Ga_y,In_{1-y})O_x$ interfacial layer at the back should effect a deterioration of solar cell parameters due to the formation of a rectifying back contact junction, blocking the diode current density.

Apart from high substrate temperatures during CIGSe deposition, GaO_x formation is also promoted by the presence of alkaline metals (Na, K) either during CIGSe growth or via post-deposition treatment (PDT) [9,19,20,27,28], and by larger ITO thickness and surface roughness [20,29]. However, Na has an ambivalent influence on the J-V characteristics [20,28–30]: Na-free solar cells with an ITO back contact show J-V characteristics equally impacted by a transport barrier for the diode current like devices with verified GaO_x formation at the rear interface. Introducing Na either as a NaF precursor or via a NaF PDT improves the solar cell characteristics, indicating a quasi-ohmic behaviour of the ITO/CIGSe back contact at T = 300 K [28,29]. However if the NaF precursor exceeds a critical thickness, the enhanced GaO_x formation neutralises the reduction of the transport barrier for the diode current by Na [19,28]. In the same vein, NaF PDT is only sufficient to create a quasi-ohmic behaviour of the devices in the case of a not to extended GaO_x layer at the back [29]. Hence, NaF PDT does not assure a quasi-ohmic behaviour for solar cells with a high thickness of the ITO back contact or if the CIGSe layer is deposited at high substrate temperatures (≥550 °C). However, when scaling up the fabrication processes to the module level, high substrate temperatures are preferred for increasing the throughput, while maintaining or improving the absorber quality, and a thick ITO (at least 800 nm) back contact with low sheet resistance is required for monolithic integration. Under these conditions, the formation of GaO_x at the ITO/CIGSe back interface and an impairment of the electrical module characteristics by a hole transport barrier is very likely. In order to avoid the formation of GaO_x, different groups [27,31,32] introduced a thin (<140 nm) functional layer (FL) based on Mo, $MoSe_2$, or $Ag_xGa_yS_z$ in between the CIGSe and the back ITO or other TCO layers. As a result, they obtained quasi-ohmic behaviour in the J-V characteristics of all devices with a FL.

In the first part of our study, we investigate the chemical stability of different ITO layers with in-situ X-ray diffraction during CIGSe growth at a nominal substrate temperature of 600 °C measured on the back side of the glass substrate. The investigated ITO back contacts differ in thickness, annealing procedure, and in the coverage with a thin Mo layer. The formation of GaO_x at the ITO/CIGSe rear interface has been examined using glow-discharge optical emission spectroscopy (GDOES) on the very same samples. In order to relate the texture and composition to the electrical properties, J-V characteristics have been measured on single solar cells.

In the second part of this study we developed semi-transparent mini-modules suitable for BIPV. At first, we transferred the results of the first part to 2.5 × 2.5 cm^2 sized mini-modules with 3 sub cells. After identifying low pressure Ar/O_2 annealed ITO with a 20 nm Mo FL as the optimum back contact, a semi-transparent 10 cm × 10 cm mini-module with 14 sub cells was prepared and tested under outdoor conditions.

2. Experimental

2.1. Manufacturing of ITO back contacts

ITO back contacts have been manufactured in-house at the Martin-Luther-University (MLU) and at the Institut de Recerca en Energia de Catalunya (IREC). To distinguish between both types of ITO the following abbreviations are employed: ITO-MLU and ITO-IREC, respectively. The glass substrates for both ITO types are 2.1 mm thick soda lime glass (SLG) coated with a 110 nm thick SiN_x diffusion barrier for Na. Deposition of ITO-MLU takes place via radio-frequency (RF) sputtering from a 90 wt.-% In_2O_3 and 10 wt.-% SnO_2 ceramic target with a working pressure of 4–6•10^{-4} mbar under an Ar flux of 14–20 sccm. Supplying a plasma power of 140 W results in an ITO growth rate of ≈12 nm/min. 300 and 800 nm ITO-MLU back contacts are fabricated without heating the substrates, after 25 and 70 min deposition times respectively. Since the substrates are not actively cooled during ITO sputtering, they are unintentionally heating up from room temperature to 30 °C in case of 300 nm and to 60 °C in case of 800 nm ITO-MLU. However, due to the unavoidable substrate heating (T > 60 °C) before CIGSe processing (see section 3.1), we expect that the temperature difference during sputtering is not decisive for the outcome of our in-situ XRD CIGSe growth studies.

Manufacturing of 800 nm ITO-IREC with and without Mo FL has been described in Ref. [14]. Compared to ITO-MLU back contacts, the ITO-IREC back contact layers are deposited onto identical SLG substrates (with a 110 nm SiN_x layer) using a reactive (with oxygen content) DC-pulsed magnetron sputtering (Alliance Concept CT100) from a 90 wt.-% In_2O_3 and 10 wt.-% SnO_2 target. Deposition time is 60 min (giving approximately 800 nm) at a nominal temperature of 400 °C, plasma power of 190 W, and with working pressure of around 2•10^{-3} mbar (30 sccm Ar, 0.5 sccm O_2). Samples are then naturally cooled-down inside the chamber and therefore are subjected to an inherent annealing step under vacuum for 6–7 h. Samples ITO-IREC + Mo include also a thin Mo layer (20 nm thick) deposited by DC magnetron sputtering (Alliance Concept AC450) just after the ITO preparation.

2.2. Single cell and module fabrication

Fabrication of CIGSe absorber layers has been conducted via co-evaporation of In, Ga, Cu, and Se from elemental sources in vacuum following the 3-stage sequence invented by Gabor et al. [33]. Incorporation of Na into the CIGSe layer has been performed directly after CIGSe deposition via NaF post-deposition treatment (PDT). For the ITO-IREC + Mo sample, the Mo layer is selenized during the manufacturing

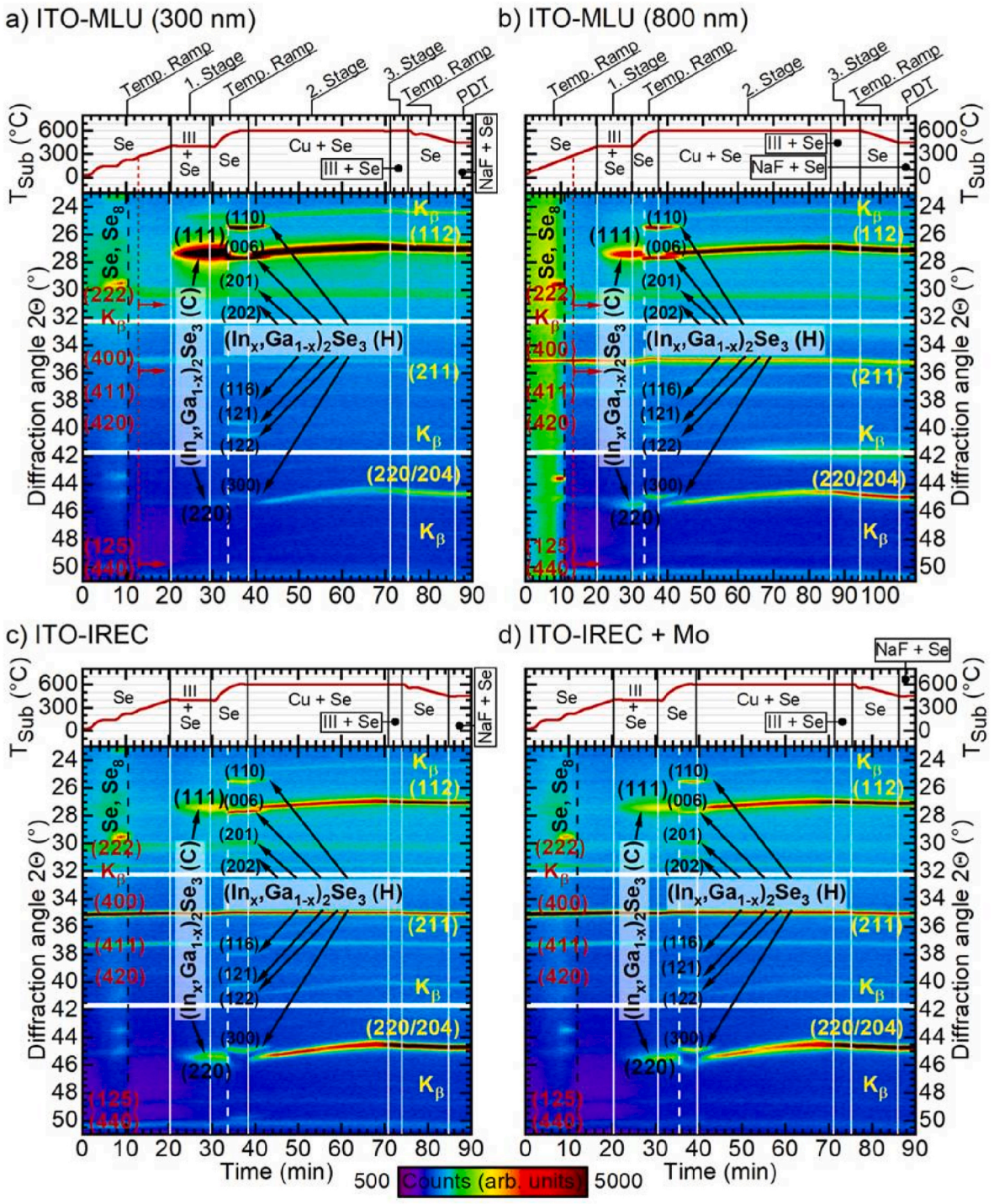

Fig. 1. Colour coded in-situ XRD pattern monitored in real time during CIGSe growth on (a) 300 nm ITO-MLU, (b) 800 nm ITO-MLU, (c) ITO-IREC (800 nm), and (d) ITO-IREC + Mo as a function of process time. On top of each colour map the substrate temperature T_{Sub} is plotted. The process stages are labelled on top of the T_{Sub} plots in (a) and (b). PDT stands for post-deposition treatment with NaF. Black and white solid lines are indicating the begin or end of each stage. Elemental fluxes during particular process stages are labelled in the particular T_{Sub} plots. III signifies the group III elements In and Ga. Within the XRD colour maps, diffraction reflexes of ITO are indicated by red indices on the left. Yellow indices on the right are characterising CIGSe reflexes and black indices are related to the cubic (C) or hexagonal (H) $(In_x,Ga_{1-x})_2Se_3$ precursor with $x \approx 0.5$. The onset of double peaks due to re-crystallisation of ITO-MLU is characterised by the red dashed line and red arrows in (a) and (b). Black dashed lines before the 1st stage are characterising the re-evaporation of Selenium and white dashed lines in between the 1st and 2nd stage are indicating the phase transition of the $(In_x,Ga_{1-x})_2Se_3$ precursor. (For interpretation of the references to colour in this figure legend, the reader is referred to the Web version of this article.)

process of the CIGSe layer.

2.2.1. In-situ XRD experiments and single solar cells

The final thickness of CIGSe absorbers from growth experiments with in-situ XRD is 1 ± 0.1 μm, having received a ≈4 nm NaF-PDT at a substrate temperature of 450 °C. During CIGSe deposition we used for the 2nd and 3rd stage 600 °C, which is the maximal achievable substrate temperature with our in-situ system. The progress of substrate temperature over the complete CIGSe deposition process is depicted in Fig. 1. In terms of material composition, the CIGSe layers revealed an integral [Ga]/([Ga] + [In]) = GGI ratio of 0.45 ± 0.05 and an integral [Cu]/([Ga] + [In]) = CGI ratio of 0.80 ± 0.10 obtained from GDOES depth profiles. Deviations in thickness, GGI, and CGI are due to the non-rotating substrate holder enabling in-situ XRD measurements. Subsequent processing of CIGSe absorbers to complete solar cells has been conducted by wet chemical deposition of a 50 nm CdS layer followed by sputtering a 100 nm intrinsic ZnO layer and a 300 nm ITO layer on top as the front emitter, resulting in a layer sequence of ITO+(Mo)/CIGSe/CdS/i-ZnO/ITO. For electrical contacting the cells were covered with a Ni/Al/Ni metal grid. Cell definition was performed via wet chemical etching of the window layers with 10% hydrochloric acid, resulting in cell sizes ranging from 0.15 to 0.35 cm^2.

2.2.2. Mini-modules

Before CIGSe deposition, P1 scribing of the ITO and ITO + Mo-FL back contacts has been carried out with a UV diode laser (355 nm, 0.85 W, 150 kHz, 25 μm), defining electrically isolated sub cells with a width of 6.5 mm. Accordingly, 2.5 × 2.5 cm^2 mini-modules have 3 sub-cells with a length of 20 mm and 10 cm × 10 cm mini-modules consist of 14 sub cells with a length of 9.5 cm. For mini-module fabrication, the CIGSe absorber thickness was increased to 2 μm. In order to reduce the probability of GaO_x formation the maximum substrate temperature for CIGSe deposition on 2.5 × 2.5 cm^2 substrates was decreased from 600 °C (in-situ XRD) down to 540 °C. Incorporation of Na has been realized by a 2 nm NaF pre-cursor layer and an 8 nm NaF-PDT. Furthermore, we applied additional doping of the CIGSe layers with potassium by means of KF precursor layers (see section 3.4) and 8 nm KF-PDT. With the knowledge that solar cells with ITO-IREC + Mo are not affected by GaO_x formation at the rear interface, CIGSe deposition on 10 cm × 10 cm substrates solely coated with an ITO-IREC + Mo back contact has been performed with a maximum substrate temperature of 625 °C. K and Na doping was performed by 2 nm precursor layers of NaF and KF each and a PDT with 8 nm NaF and KF each. After CIGSe deposition, the devices have been coated with 50 nm CdS by chemical bath deposition and structured by mechanical scribing of the P2 for sub-cell interconnection. The front side TCO was identical to solar cells from in-situ XRD experiments. P3 cell separation and removal of the solar cell stack has been performed again by mechanical scribing, using a scalpel. To ensure residue-free surfaces of the exposed back contact, a mechanical cleaning step with a fibre glass pen was performed. By measuring Raman on the exposed back contacts no CIGSe residuals were found, which is shown in our recent publication [14].

Metal bars for electrical contacting were made from silver varnish in the case of 2.5 × 2.5 cm^2 mini-modules and from soldered indium in the case of 10 cm × 10 cm mini-modules. Encapsulation for outdoor testing has been realized by bonding a 10 cm × 10 cm glass slide on top of the module. The applied glue Sikasil WS-605S also acted as environmental sealing of the module.

3. Results and discussion

3.1. Texture and stability of ITO back contacts

During CIGSe processing, the ITO back contact is exposed to a selenium atmosphere at high temperatures of 540–625 °C. To investigate the chemical stability of different ITO back contacts, in-situ X-ray diffraction (XRD) has been applied in real time during CIGSe growth. (For details of the in-situ XRD setup and measurement we refer to Refs. [34,35].) Fig. 1 shows the colour coded XRD patterns monitored with a time resolution of 42 s during deposition of CIGSe on (a) 300 nm ITO-MLU, (b) 800 nm ITO-MLU, (c) ITO-IREC (800 nm), and (d) ITO-IREC + Mo. For identification of the ITO peaks, the ICDD-card No. 04-023-7387 (based on lattice parameters found in Ref. [36]) has been used. In order to investigate the ITO stability against high substrate temperatures for a longer time period, the 2nd stage of the CIGSe process has been extended from typical 15 min to more than 30 min. XRD pattern recording was stopped after the NaF-PDT sequence since no further change of XRD peaks and intensities was observed.

In Fig. 1 a) the peak intensity of the thin ITO-MLU initially suggests a preferred (222) orientation. However, the (222) peak is located on a broad background peak which originates from the amorphous SLG substrate (see Supporting information, Figure S - 1). In order to correct for the background effect, Table 1 presents the results of a peak analysis (PDXL software) of the diffraction pattern from a Θ-2Θ scan at room temperature before CIGSe processing. The peak areas of the (222) and (400) reflexes of the 300 nm ITO-MLU are nearly identical. By normalizing these peak areas to the respective intensities in the ICDD-card No. 04-023-7387, a factor $A_{N,m}$ for the normalized area is obtained for each peak. This normalisation method accounts for the different structure factor of each peak. Comparing the $A_{N,m}$ values of the (222) and (400) reflexes for the different ITO back contacts in Table 1, we conclude for a slightly preferential (400) orientation of the 300 nm ITO-MLU layer. The increased thickness of the 800 nm ITO-MLU layer, however, results in a strong (400) texture (see also Fig. 2).

In case of the high temperature (400 °C) processed ITO-IREC (800 nm) an even higher peak of the (400) reflex can be observed in Table 1. The trend of increasing peak height of the (400) reflex with higher ITO thickness and with higher substrate temperature during sputtering was already visible in Fig. 1. The smaller FWHM values of ITO-IREC point towards larger grains and an enhanced crystallinity due to high substrate temperatures during sputtering [37,38]. The pronounced (400) orientation has been attributed to the high stability of (400) textured crystallites against re-sputtering during ITO deposition [39]. Alternatively, a preferential (400) orientation has been ascribed to oxygen depletion during ITO sputtering [39].

After air-annealing the 300 nm ITO-MLU at 600 °C for 60 min we found a predominant (400) orientation, albeit an increase of all reflexes (see Fig. 2). The annealing procedure reduced the FWHM values by a factor of 2, indicating re-crystallisation (see Supporting information, Figure S - 2). The peak centres of all reflexes shifted from −0.3° to +0.2° if referenced to the ICDD data. This indicates a change from lateral compressive to tensile stress of the film. Air-annealing of the 800 nm ITO-MLU lead to an equivalent shift to higher angles and increase in peak height and area, but primarily for the (222) reflex. On the other hand, the peak characteristics of the initial (400) reflex was almost unaffected after air-annealing, possibly due to a reduced annealing time of 10 min or a higher initial crystallinity of the thicker films. However, a shoulder was forming at the high angle side of the (400) reflex with an identical peak centre of ≈35.6° as the (400) reflex of the 300 nm ITO-MLU films air-annealed for 60 min (see Supporting information Figure S - 2). Due to this shoulder, $A_{N,(400)}$ of the air-annealed 800 nm ITO-MLU films increases compared to the as fabricated films, indicated by the dotted arrows in Fig. 2 a).

The reactively sputtered ITO-IREC shows in the region of the (222) reflex two distinct peak maxima designated with $(222)_1$ and $(222)_2$ in Table 1. The origin of the double peak is not fully clear, it is only observable for the (222) reflex. All other peaks especially at higher diffraction angles reveal single peak behaviour. Close to the (222) ITO reflex, the (003) reflex at 30.24° and the (211) reflex at 30.56° of the rhombohedral $In_4Sn_3O_{12}$ phase (ICDD-card No. 01-088-0773 or [40]) are located. It is reported that $In_4Sn_3O_{12}$ has a high Hall mobility of 20 $cm^2(Vs)^{-1}$ and optical transparency [41], which may explain the high

Table 1
XRD peak data of the different ITO substrates obtained by Θ-2Θ scans at room temperature before CIGSe processing.

Peak properties	ITO-MLU				ITO-IREC		
	d = 300 nm		d = 800 nm		d = 800 nm		
	(222)	(400)	(222)	(400)	$(222)_1$	$(222)_2$	(400)
Diffraction centre [°]	29.91 ± 0.08	35.03 ± 0.08	30.09 ± 0.11	35.12 ± 0.04	30.11 ± 0.02	30.50 ± 0.08	35.18 ± 0.03
Height [counts]	220 ± 121	497 ± 165	133 ± 35	5047 ± 886	196 ± 91	254 ± 110	7956 ± 984
FWHM [°]	0.462 ± 0.037	0.187 ± 0.025	0.482 ± 0.099	0.208 ± 0.025	0.283 ± 0.028	0.419 ± 0.024	0.168 ± 0.013
Area [°•counts]	129 ± 60	127 ± 56	80 ± 31	1216 ± 193	59 ± 23	119 ± 52	1678 ± 334
Normalized area $A_{N,m}$ [a)]	0.129 ± 0.060	0.423 ± 0.187	0.080 ± 0.031	4.053 ± 0.643	0.059–0.176 [b)] ± 0.069	0.119 ± 0.052	5.593 ± 1.113

[a)] Normalisation to the identified powder intensities I_m with $I_{(222)} = 1000$ and $I_{(400)} = 300$ for ITO (ICDD-card No. 04-023-7387).
[b)] Normalisation to the identified powder intensities of ITO and $In_4Sn_3O_{12}$ with $(222)_1 \rightarrow (003)$ and $(222)_2 \rightarrow (211)$, giving $I_{(003)} = 335$ and $I_{(211)} = 1000$ for $In_4Sn_3O_{12}$ (ICDD-card No. 01-088-0773).

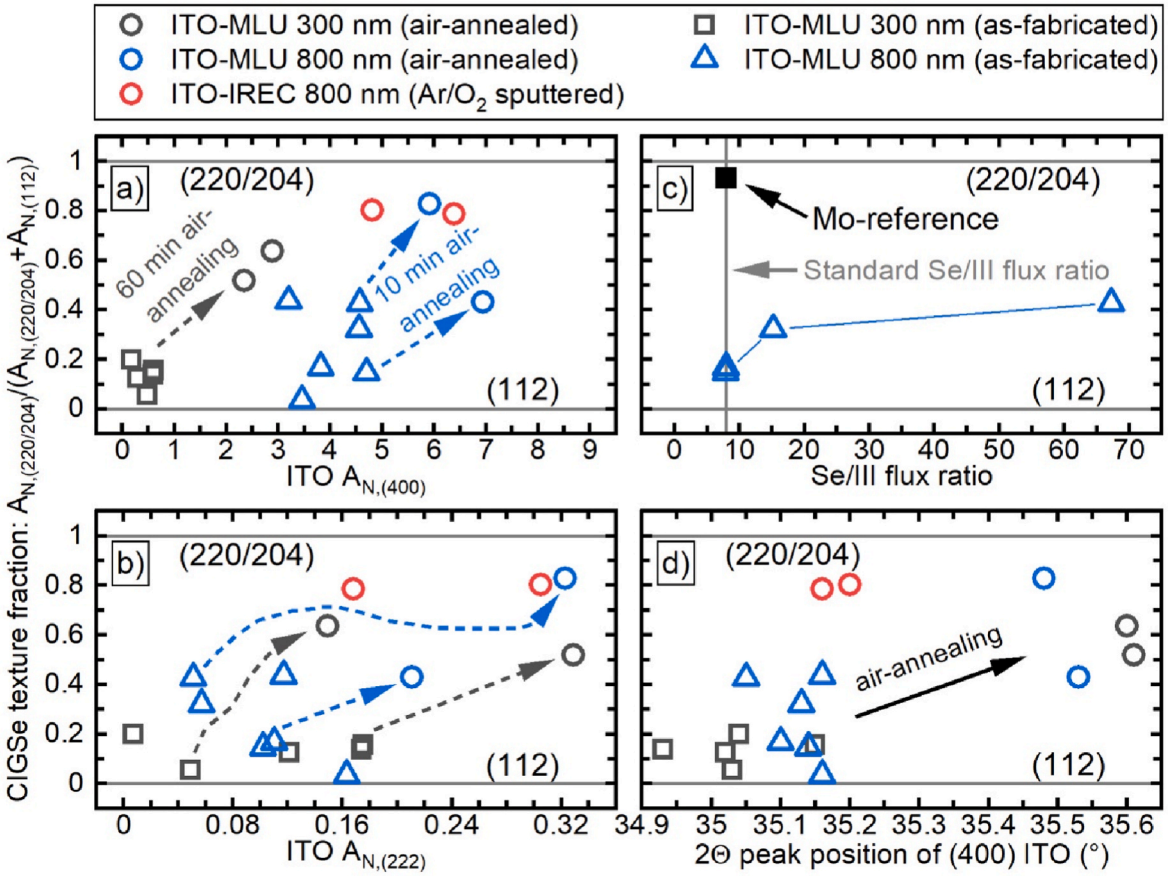

Fig. 2. (a), (b) Final texture of CIGSe films grown on ITO substrates differing in thickness, sputtering and annealing conditions. The ITO crystallinity has been evaluated in terms of $A_{N,(400)}$ in (a) and $A_{N,(222)}$ in (b). $A_{N,m}$ values of ITO have been obtained from XRD Θ-2Θ scans measured at room-temperature before CIGSe processing and were normalized to the respective powder intensity. The texture of the final CIGSe layer is evaluated in terms of the fraction of $A_{N,m}$ of the most pronounced CIGSe orientations with m = (112) and m = (220/204) neglecting other orientations. $A_{N,(220/204)}$ has been obtained by averaging the (220) and (204) powder intensities. The $A_{N,m}$ values for CIGSe are derived from XRD Θ-2Θ scans at room-temperature after CIGSe processing. Scattered lines with arrows are indicating the change in crystallinity of ITO and CIGSe texture due to air-annealing. The connected data points represent identical ITO layers, sputtered at the same time. (c) Final CIGSe texture as a function of the ratio of the Se flux to metal III flux during the 1st stage of the CIGSe process on 800 nm thick ITO-MLU. (d) Final CIGSe texture as a function of the 2Θ peak positions of the (400) reflex in XRD Θ-2Θ scans measured at room-temperature before CIGSe processing.

conductivity and transparency of ITO-IREC samples. However, the ITO-IREC films have been sputtered from ceramic targets with 90 wt.-% In_2O_3 and 10 wt.-% SnO_2. Due to the lack of Sn, it is not possible to convert the complete ITO film into the $In_4Sn_3O_{12}$ phase. Thus, we assume – considering the results of González et al. [42] – that the final ITO-IREC film has only a minor fraction of $In_4Sn_3O_{12}$ phase.

Before the CIGSe process started, the samples were heated from room temperature to 400 °C under a constant Se supply. For temperatures <225 °C, the formation of a Se-layer on the substrate surface is visible in Fig. 1. The XRD reflections are matching predominantly hexagonal Se (ICDD-card No. 01-086-2246 or [43]) and monoclinic Se_8 (ICDD-card No. 01-086-2246 or [44]). Surpassing a substrate temperature of 225 °C, the XRD reflections of Se are vanishing, indicated by the white dashed line. This can be attributed to selenium re-evaporation from the substrate surface. Reaching a substrate temperature of 270 °C, the ITO-MLU layers in Fig. 1 a) and b) begin to re-crystallize. After surpassing 270 °C, the diffraction pattern of ITO-MLU exhibits for all reflexes an additional peak maximum at higher angles, hereon designated as double-peaks. (A

comparison of ITO XRD reflexes before and after CIGSe processing as well as before and after vacuum-annealing is given in Figure S - 3 of the Supporting information.) The red dashed lines and arrows at ≈ 13 min indicate the starting point of the appearance of these double-peaks. The hypothesis, that the additional peaks are due to re-crystallisation was confirmed by monitoring similar double peaks with in-situ XRD in real time during annealing of an identical ITO-MLU substrate in vacuum shown in Figure S - 4 of the supporting information. During vacuum annealing the substrate has been exposed to a similar temperature sequence as applied during the CIGSe processes in Fig. 1. Also in this case, double peaks occur after surpassing 270 °C on the heating ramp. Thereafter, the ITO reflexes of the XRD pattern did not change further with increasing temperature or time and the annealing experiment was stopped after holding the substrates at 600 °C for 10 min. After annealing in vacuum the transparency of the ITO-MLU was enhanced and the conductivity was higher by one order of magnitude, confirming a higher degree of film crystallinity, which is also reported in Refs. [45–47].

XRD double peaks after post-annealing in vacuum of ITO layers have been observed by Neerinck and Vink [48] as well. With depth dependent grazing incidence asymmetric Bragg XRD in combination with cross-sectional transmission electron microscopy they were able to relate the occurrence of the double peaks to the formation of an ITO double layer with different stress states of the sub-layers. The bottom layer is found to be stress-free with a higher diffraction angle, whereas the top layer exhibits in-plane compressive stress resulting in a lower diffraction angle [48]. Relating the findings of Neerinck and Vink to our experimental data of ITO-MLU, we conclude that a more tensile stressed sublayer is formed during heating up the substrates before the beginning of the actual CIGSe process. The re-crystallisation of the ITO-MLU takes place within a very short time frame of 2 min. Subsequently, throughout the whole CIGSe process no further changes in the XRD pattern of the ITO-MLU occur in Fig. 1 a) and b). In the case of the high temperature processed ITO-IREC, the XRD-reflexes of ITO in Fig. 1 c) and d) show no changes over the complete process time. This holds for the air-annealed ITO-MLU films as well. In summary, we find the simultaneous occurrence of two phenomena when ITO films are annealed in vacuum (e.g. in the course of CIGSe growth), namely the formation of ITO double peaks and the preferred CIGSe 112 texture. However, based on our experiment it is not clear if the latter results from the former phenomenon.

All emerging diffraction peaks during CIGSe growth can be assigned either to the cubic (ICDD-card No. 04-003-9445 or [49]) or hexagonal (ICDD-card No. 01-087-1482 or [50]) $(In_x,Ga_{1-x})_2Se_3$ precursor layer and with beginning of the 2nd stage to the tetrahedral $Cu(In_x,Ga_{1-x})Se_2$ layer (ICDD-card No. 00-062-0710).

3.2. Texture of CIGSe grown on ITO

After the 1st stage of the CIGSe process in Fig. 1 the substrates are heated-up within ≈10 min from 400 °C to 600 °C under constant selenium supply. During this period, a phase transition of the $(In_x,Ga_{1-x})_2Se_3$ precursor from cubic to hexagonal occurs. The lattice change of the precursor is marked by the white dashed line located at ≈ 33 min in Fig. 1 a) – d). A preferential (111) orientation of the cubic $(In_x,Ga_{1-x})_2Se_3$ precursor in Fig. 1 a) results in a preferential (110) and (006) oriented hexagonal $(In_x,Ga_{1-x})_2Se_3$ phase. This leads to a final CIGSe layer with preferential (112) texture. Preferential (112) texture of the CISe layer grown from a (006) textured hexagonal In_2Se_3 precursor has been observed before [51]. In contrast, a (300) hexagonal $(In_x,Ga_{1-x})_2Se_3$ orientation leads to a (220)/(204) orientation of CIGSe [51]. It was reported that a (300) hexagonal $(In_x,Ga_{1-x})_2Se_3$ layer on Mo substrates can be achieved by a high selenium/metal flux ratio (>7). A (220/204) texture of the CIGSe absorber is thought to be beneficial for the opto-electronic properties of the final solar cell [52–54].

Fig. 2 gives the texture fraction $A_{N,(220/204)}/(A_{N,(112)} + A_{N,(220/204)})$ of the CIGSe (112) and (220/204) main reflexes, neglecting other crystallographic directions, as a function of different variables. The data have been obtained from XRD Θ-2Θ scans at room temperature after CIGSe processing. For calculating the texture fraction the peak intensities have been normalized with the powder peak areas $A_{N,m}$ in order to correct for different structure factors of the reflections. A texture fraction of >0.5 means a predominant (220/204) oriented CIGSe film, while <0.5 means predominant (112) orientation. The abscissa in Fig. 2 a) and b) represent the powder normalized peak areas $A_{N,m}$ of the ITO (400) and (222) main reflexes, respectively.

First, we consider the sample grown on molybdenum in Fig. 2 c). In agreement with earlier results [55], this sample shows a preferred (220)/(204) orientation as a result of the standard high Se/metal flux ratio of ≈8. However, in Fig. 2 a), CIGSe films grown on non-annealed 300 nm ITO MLU exhibit a preferred (112) texture. This result was demonstrated 5 times during identical CIGSe processes on as-fabricated 300 nm thick ITO-MLU in our in-situ XRD process chamber with standard selenium/metal III flux ratio of ≈8 (see grey squares in Fig. 2 a). In Fig. 2 c), an identical preferred (112) texture we find for CIGSe layers grown on as fabricated 800 nm ITO-MLU too. Even a higher Se/metal flux ratio does not substantially increase the fraction $A_{N,(220/204)}/(A_{N,(112)} + A_{N,(220/204)})$ in Fig. 2 c). Hence, the ITO layer has a dominant influence on the CIGSe texture. In Fig. 1 a), it can be seen that the CIGSe texture already was predefined by the hexagonal $(In_x,Ga_{1-x})_2Se_3$ precursor texture – in accordance with the general texture relation between CIGSe and $(In_x,Ga_{1-x})_2Se_3$ as explained above. Therefore, the ITO influence on CIGSe is mediated via the $(In_x,Ga_{1-x})_2Se_3$ precursor texture.

Next, we consider the effect of annealing ITO in air and reactive sputtering of ITO with an Ar/O_2 flux-ratio of 60:1, respectively. In case of 300 nm ITO-MLU, the ITO $A_{N(400)}$ in Fig. 2 a), increases strongly after air-annealing by nearly one order of magnitude. Since for the annealed ITO samples both $A_{N,(400)}$ and $A_{N,(222)}$ are found to be increased, we conclude a higher crystallinity of the ITO layer. CIGSe layers in two separate runs grown on air-annealed 300 nm ITO-MLU (grey circles) show an enhanced (220/204) texture of the CIGSe layers. However no general influence of the ITO texture and crystallinity on the CIGSe orientation can be concluded, since as-fabricated 800 nm ITO-MLU has a preferred (400) texture with varying crystallinity, but the CIGSe films grown on top of these layers do not show a clear texture trend in Fig. 2 a). This suggests that the final CIGSe texture is not a function of the preferred (400) orientation and of the varying crystallinity of the underlying ITO film. Rather, the annealing in air or Ar/O_2 reactive sputtering of ITO determines that the CIGSe films are not (112) oriented but are random or preferentially (220)/(204) oriented. This is depicted in Fig. 2 a) and 2 b), the latter showing the influence of the ITO (222) preference. In Fig. 1 c) and d) the $(In_x,Ga_{1-x})_2Se_3$ precursors grown on Ar/O_2 reactively sputtered ITO-IREC, independent whether bare or covered with Mo, show a higher proportion of (220) oriented domains for the cubic phase. After the cubic/hexagonal phase transition this translates into a lower (110) and (006) orientation, giving a proportionally higher (300) textured hexagonal $(In_x,Ga_{1-x})_2Se_3$ precursor. Consequently, the texture of the final CIGSe layer exhibits an enhanced (220/204) orientation compared to CIGSe layers grown on as-fabricated ITO-MLU.

We conclude that annealing ITO back contacts in an oxygen containing atmosphere facilitates an enhanced (220/204) orientation of the CIGSe layer grown on top. The wide range of CIGSe textures grown on thick 800 nm as-fabricated ITO-MLU in Fig. 2 (blue triangles) may indicate some variation of the oxygen content of the ITO films, either due to the modification of the sputter target and/or due to the enhanced incorporation of residual oxygen gas because of an extended sputtering time.

Now we turn to the remaining question of the oxygen influence on the texture of the $(In_x,Ga_{1-x})_2Se_3$ precursor (and the later CIGSe). A reduced oxygen content in the ITO surface may modify the diffusivity of ad-atoms on the surface of the ITO film. At the beginning of the growth process surface diffusivity facilitates the coalescence of initially formed

particles with a certain orientation and thereby the texture of the final film [56]. Hence, the texture of the $(In_x,Ga_{1-x})_2Se_3$ precursor can be a function of the ITO surface diffusivity. However, also strain in the ITO layer may influence the $(In_x,Ga_{1-x})_2Se_3$ precursor growth, since strain is assumed to modify the ITO surface energy. By virtue of minimizing interface energy and strain of particles accumulating from the vapour phase, the surface energy of the substrate can affect the preferred film orientation in the initial phase of film growth strongly [56]. Accordingly, it has been shown by Yoon et al. [57] that increasing tensile strain of Mo back contacts ensures a higher (300) orientation of the $(In_x,Ga_{1-x})_2Se_3$ precursor as well as a higher (220/204) orientation of the final CIGSe film. In Fig. 2 d), the XRD peaks of the (400) reflex are shifting to higher angles after air-annealing. This indicates, with respect to the ITO (400) peak position located at $2\Theta \approx 35.5°$ in powder diffractograms, a reduced compressive strain within the ITO back contact. To which extent this effect, the crystallinity of the ITO or the diffusivity of the ITO surface are responsible for the enhanced (220/204) CIGSe texture on Ar/O_2 reactively sputtered and air-annealed ITO films cannot be resolved completely within our study. This is so, because as shown in Fig. 2 d) a compressive stress-state for ITO-IREC can be observed. The ITO-IREC samples exhibit compressive stress but still have a preferred 220/204 texture. However, for achieving a preferred (220/204) CIGSe texture, which is beneficial for solar cell quality, annealing of Ar-sputtered ITO back contacts in an oxygen containing atmosphere seems to be indispensable. Admixing of O_2 during Ar sputtering of ITO back contacts also leads to a preferred (220/204) texture of grown CIGSe films on this type of back contacts. Whether increasing the partial pressure of O_2 during ITO sputtering enhances the preferential (220/204) CIGSe texture is still part of ongoing research.

3.2.1. Functional Mo layer at the rear interface

For a long time it is known that gallium oxide (GaO_x) forms on an ITO surface during CIGSe growth at high substrate temperatures >500 °C [15]. Following the proposal of Rostan et al. [31] and Nakada [27], we decided to cover the higher quality ITO-IREC with a very thin Mo layer (ITO-IREC + Mo), in order to prevent the formation of GaO_x. The in-situ XRD colour map recorded during the growth of CIGSe on this back contact is shown in Fig. 1 d), where the (110) reflex of Mo at 40.51° (ICDD-card No. 00-004-0809) can only be guessed. However, by comparing detailed Θ-2Θ scans of ITO-IREC and ITO-IREC + Mo, the (110) Mo peak becomes visible. A peak analysis with the PDXL software reveals ≈40.7° for the peak centre, indicating a compressive stress state of the thin Mo layer. On SLG compressive strained Mo layers tend to delaminate [58]. However, no issues related to the adhesion of Mo on ITO occurred throughout our study. A former study revealed the formation of $MoSe_2$ during CIGSe growth out of the Mo layer [14]. However, here the $MoSe_2$ structure was not detected by XRD, possibly due to low thickness.

Comparing the ITO peaks of ITO-IREC and ITO-IREC + Mo, we find a shift of all peaks by ≈ 0.03° towards lower angles in the case of ITO-IREC + Mo. This indicates an increased tensile stress state of the ITO layer triggered by the application of the thin Mo layer.

If it comes to the CIGSe growth there is no difference observable between bare ITO-IREC and ITO-IREC + Mo in Fig. 1 c) and d). The final texture of the CIGSe layers is identical in both cases with a preferred (220/204) orientation with $A_{N,(220/204)}/(A_{N,(112)} + A_{N,(220/204)}) \approx 0.8$. This suggests that the preferential orientation of the CIGSe layer is predetermined by the ITO back contact. Rather, it prefigures that the stress-state and not the surface diffusivity of ITO determines the final CIGSe texture. Since, because of the Mo layer, the $(In_x,Ga_{1-x})_2Se_3$ precursor is not able to come into contact with the ITO surface. But, the (220/204) texture fraction of the final CIGSe layer is not as high as observed on the Mo-reference in Fig. 2 c). Hence, we interpret the stress-state of the ITO back contact as decisive for the final orientation of the CIGSe layer. Similar texture manipulations of CIGSe by varying the stress-state of the substrate have been previously demonstrated for Mo back contacts [57,59,60].

3.3. GaO_x formation at the rear interface

Measured J-V-curves with characteristic parameters of the best cell of each particular back contact are presented in Fig. 3.

All solar cells, shown in Fig. 3, exhibit a poor short circuit current density (J_{SC}). J_{SC} was obtained from external quantum efficiency measurements, which reveal reduced collection efficiencies over the

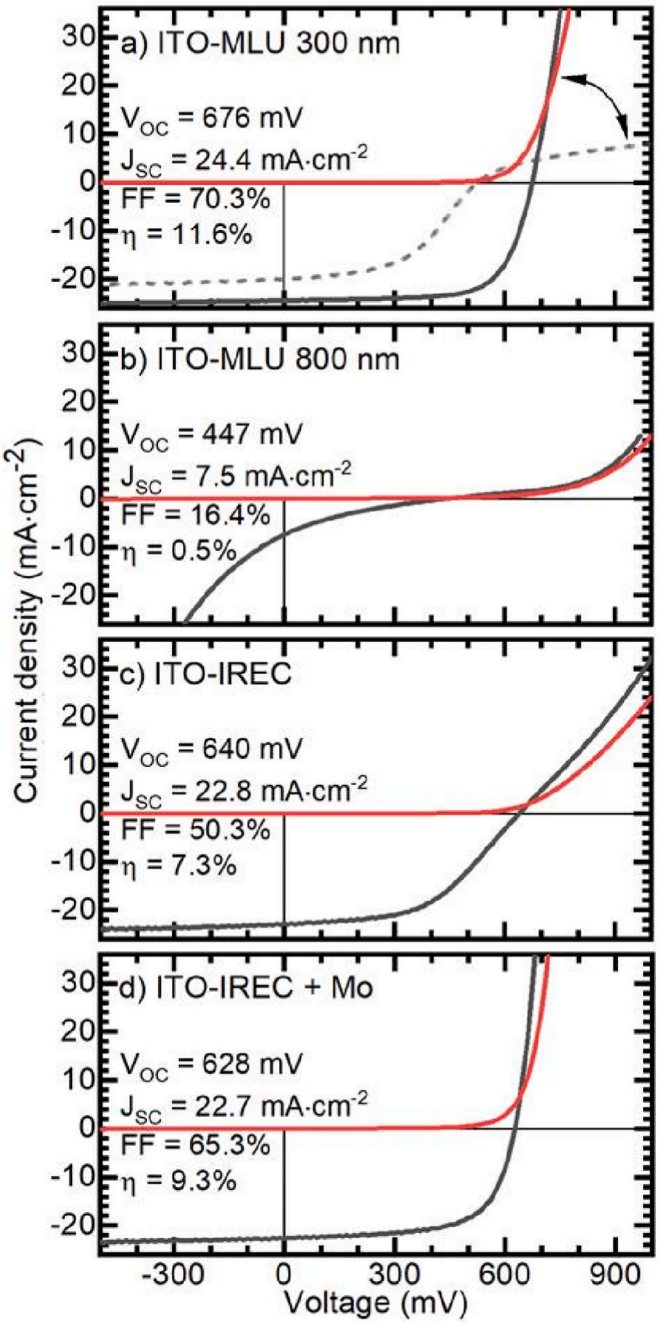

Fig. 3. J–V characteristics of solar cells with CIGSe absorbers from in-situ XRD experiments, reported in sections 3.1 and 3.2. Short circuit current densities were obtained from external quantum efficiency measurements. Red curves are dark characteristics, black curves were measured under 1 sun illumination. The dashed curve is the J-V characteristics of a solar cell from a different batch. (For interpretation of the references to colour in this figure legend, the reader is referred to the Web version of this article.)

complete wavelength range (compare Figure S - 5). We attribute this to parasitic absorption of the front ITO and/or i-ZnO window layer caused by contamination of the particular sputter target. Nevertheless, anomalies of J-V characteristics visible in Fig. 3 b) and c) are not explainable with an inferior front side TCO and can be reproduced with an intact front side TCO (see bare ITO-IREC in Fig. 5). Solar cells with 800 nm ITO-MLU back contacts from eight different CIGSe batches exhibit distorted J-V curves under illumination as shown in Fig. 3 b). Among all of our in-situ XRD batches, we observed the best J-V parameters on solar cells with a 300 nm ITO-MLU back contact, shown in Fig. 3 a). However, these results are not reliably reproducible and solar cells on 300 nm ITO-MLU from different batches exhibit a roll-over in the 1st quadrant as shown by the dashed curve. A roll-over in combination with a reducing photocurrent density upon increasing bias-voltage are symptoms of a potential barrier for holes at the back contact [61,62].

In the case of the bare ITO-IREC sample shown in Fig. 3 c), dark and illuminated J-V curves suggest an increased series resistance for this device. In view of a higher conductivity of ITO-IREC (2–3 Ω/sq., measured with Van der Pauw method [63]) compared to 300 nm ITO-MLU (5–6 Ω/sq.) and a simultaneously processed front side TCO, we attribute the apparent high series resistance to the presence of a transport barrier at the back contact, similar to J-V curves impacted by a back contact barrier in Ref. [19]. Comparing the reduced slopes of the diode-current of bare ITO-IREC samples with the roll-over of 300 nm ITO-MLU samples concludes for a higher permeability for holes of the surmised transport barrier formed on ITO-IREC. The latter observation

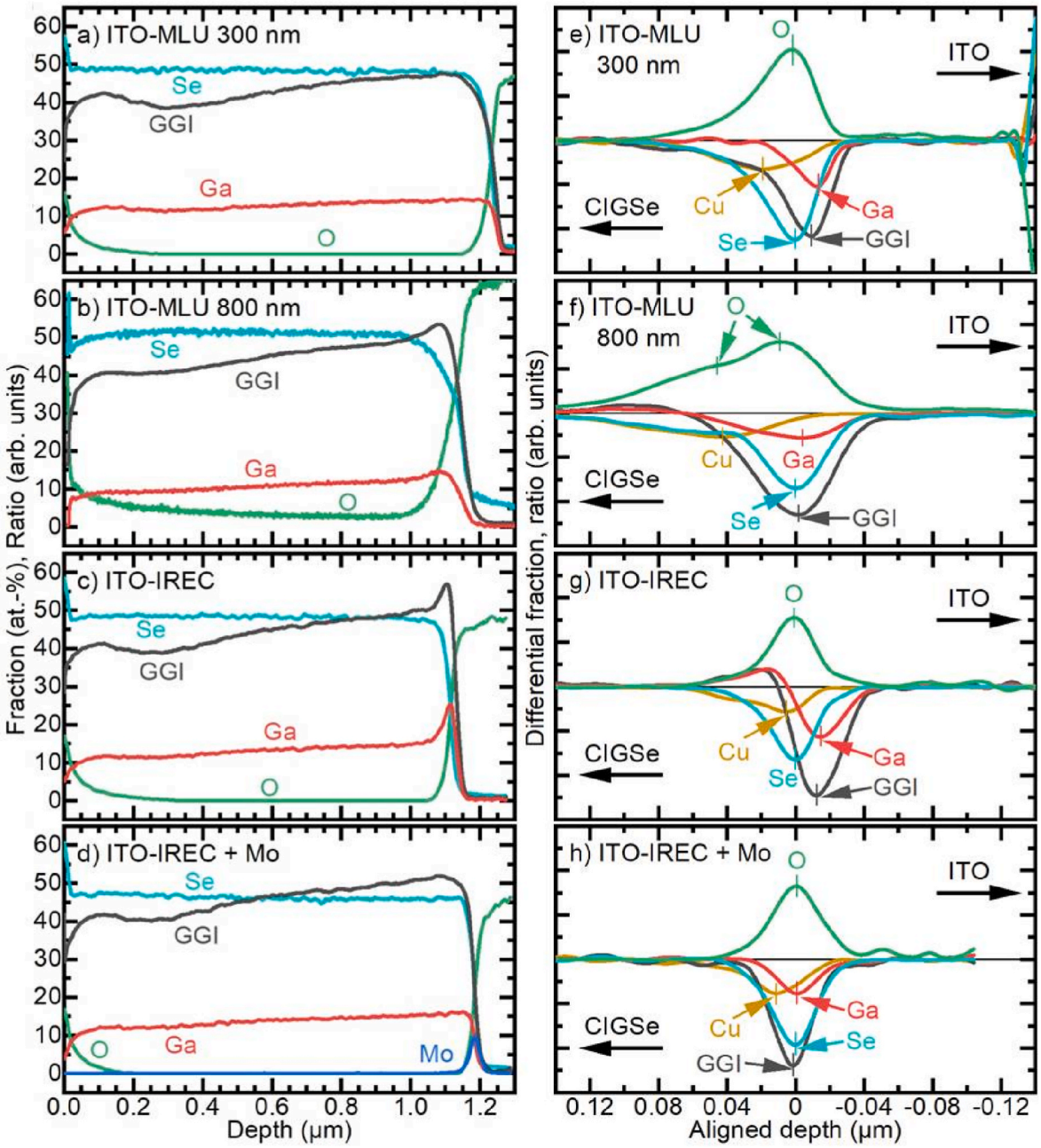

Fig. 4. (a)–(d) Elemental and GGI depth profiles of CIGSe absorbers grown on different back contacts as indicated with a maximum substrate temperature of 600 °C. The depth profiles have been measured by GDOES after partially removing the window layers from completed solar cells. (e)–(h) Differential representation of the data in the vicinity of the CIGSe/back contact interface. For the sake of comparability, the differential profiles have been aligned by shifting the depth scale, so that the Se minimum is located at 0 for each sample.

could be explained by a locally shunted back contact barrier in case of ITO-IREC. This is supported by the observation of a still strongly reduced, but non-linear slope (convex) of the diode-current for V > 1.5 V (not shown) and a slight kink in the 1st quadrant at ≈ 800 mV. Local shunts in a transport barrier can lead to apparent resistance effects: The hole current density gets an additional, now lateral component towards or away from the regions of shunts in the barrier, resulting in an apparently increased series resistance, but no roll-over. Also, the higher open circuit voltage (V_{OC}) of bare ITO-IREC compared to ITO-IREC + Mo is maybe explained by a barrier for the majority charge carriers at the back contact. For this, however, additional local shunts in the CIGSe layer have to be assumed which upon barrier action of the ITO-IREC become passivated. This would be similar as the assumed passivation action of the intrinsic layer at the front contact [64].

In order to discuss the origin of such a hole barrier, representative elemental depth profiles of CIGSe/back contact stacks measured with glow-discharge optical emission spectroscopy (GDOES) are depicted in Fig. 4 a) - d). A segregation of Ga at a depth of ≈1 μm, where the CIGSe/ITO rear interface is located, can be observed most significantly for the bare ITO-IREC. We attribute this Ga accumulation to a GaO_x layer formed during CIGSe growth at high substrate temperatures of 600 °C. In Fig. 4 e) - h) aligned differential elemental depth profiles in the vicinity of the CIGSe/ITO interface are shown. In these plots, a GaO_x layer would show up as a shift between the oxygen maximum (at the CIGSe/GaO_x interface) and the gallium minimum (at the GaO_x/ITO interface). This is the case for all samples except for the one with the ITO-IREC + Mo back contact. All bare ITOs exhibit a shift of the minima of the Ga signal derivatives towards the ITO layer. Consequently, we assume the presence of a GaO_x layer at the back contacts without Mo. This also holds for the 300 nm ITO-MLU samples, where the Ga accumulation does not show up in the original GDOES plot, perhaps due to a lower thickness of the GaO_x layer.

Combining electrical and structural information from Figs. 3 and 4, we conclude that the formation of a GaO_x layer at the back contact does not necessarily lead to J-V characteristics distorted by a transport barrier. This is emphasized by the different J-V curves from samples with 300 nm ITO-MLU back contact shown in Fig. 3 a) (see also Ref. [9]). The mechanism of charge carrier transport in the presence of GaO_x is not yet clear. Both an electron barrier (electrons reaching the GaO_x/CIGSe interface over a ITO/GaO_x conduction band offset) and a hole barrier (holes reaching the GaO_x/CIGSe interface over a CIGSe potential barrier) can be responsible for blocking the photocurrent. This holds vice versa for the diode current and a J-V characteristics like the one of the 800 nm ITO-MLU sample in Fig. 3 b) would be expected. Interestingly, a broadening of the differential peaks at the interface towards the CIGSe layer can be observed for this sample in Fig. 4 f), possibly pointing to an enhanced GaO_x thickness.

As pointed out in the introduction, the supply of Na is able to reduce the transport barrier at the rear interface. For the 300 nm ITO-MLU back contact, this relation holds true and a higher concentration of Na (see Figure S - 6, Supporting information) is found at the rear interface for the sample with a quasi-ohmic J-V characteristics than for the sample showing a roll-over. However, comparing J-V curves and Na concentrations of 800 nm ITO-MLU and ITO-IREC the opposite trend is found. That means, in spite of a higher Na concentration at the ITO/CIGSe interface an enhanced impact by a barrier on the J-V characteristics of 800 nm ITO-MLU is observed. This supports the theory that for an increased thickness of GaO_x the Na supply is not sufficient anymore to create shunts within the ITO/CIGSe junction.

In the case of the differential Cu fraction in Fig. 4, all samples exhibit a preceding minimum indicating a Cu depletion of CIGSe towards the back contact. However, Raman spectra measured through the

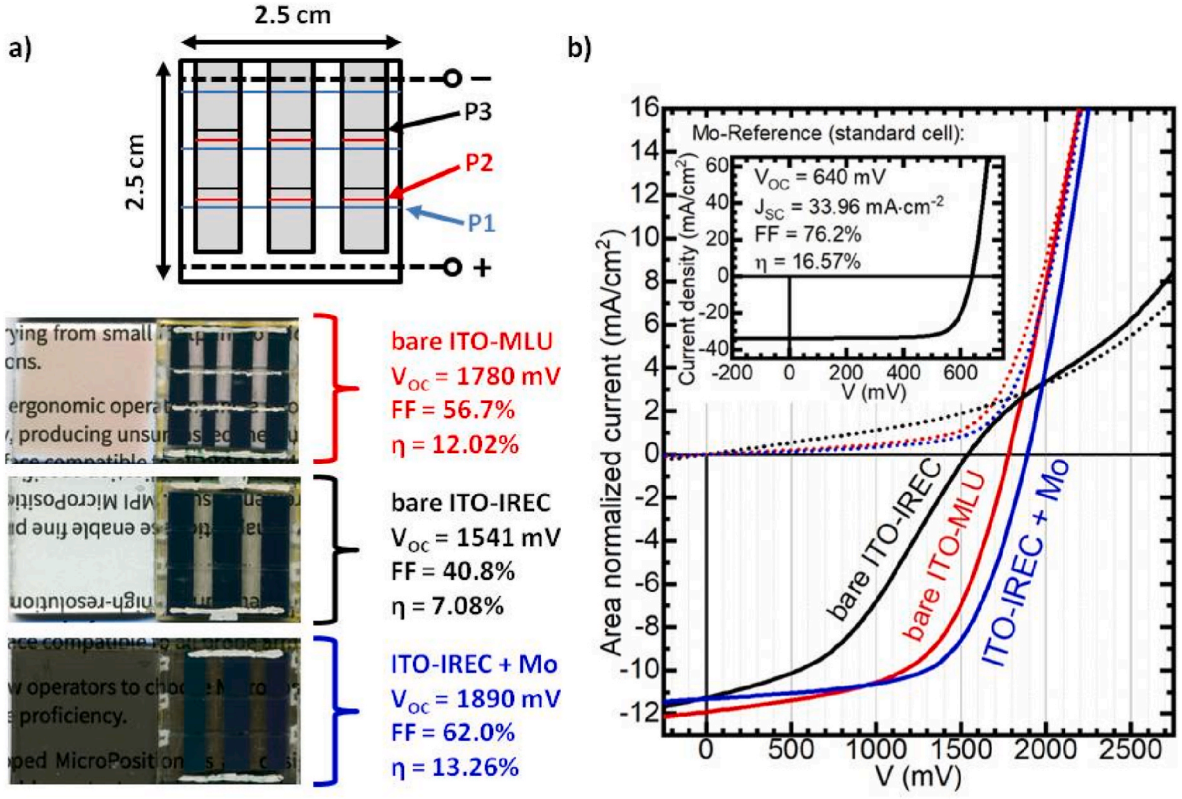

Fig. 5. (a) Schematic sketch of the circuitry of 2.5 × 2.5 cm^2 semi-transparent mini-modules and photographs of 2.5 × 2.5 cm^2 substrates with different back contacts before CIGSe processing in comparison with semi-transparent mini-modules manufactured on the same back contacts (bare ITO-MLU refers to 300 nm ITO-MLU). (b) Current-voltage characteristics of the mini-modules with current normalized to the solar active area. Inset of (b): J-V characteristics and parameters of a 0.5 cm^2 single cell with grid fingers manufactured together with the mini-modules.

transparent back contact with infrared laser excitation of 785 nm do not show a higher content of an ordered vacancy compound (OVC) at the rear interface (see Supporting information, Figure S - 7). For the ITO-MLU sample, the spectral contributions associated to OVC (around 155 cm^{-1} and in the 220-250 cm^{-1} region) are lower at the rear interface than at the front one, indicating a lower OVC presence at the rear interface [65]. For the ITO-IREC sample, these contributions are similar at the rear and at the front, indicating similar OVC content at both interfaces. Clearly, the presence of remaining metallic Mo at the back contact prevents the Raman measurements through the glass substrate, so the rear interface of ITO-IREC + Mo sample cannot be evaluated by Raman. Then, it is worth to note that the formation of an amorphous In–Se phase on ITO back contacts during the CIGSe co-evaporation process has been reported [14]. Those In–Se phases exhibit Raman signals in the 100-250 cm^{-1} spectral region [66–70]. Thus, formation of this phase could explain the higher Raman intensity in the 190-225 cm^{-1} spectral region observed at the rear interface for ITO-IREC sample. For ITO-MLU samples, the formation of this amorphous In–Se phase is also possible; however, the Raman signals from In–Se, CIGSe, and OVC cannot be discriminated in that spectral region, hence it is not possible to confirm if the observed spectral variations correspond to In–Se formation or to changes in the other phases. In any case, it appears that the formation of this In–Se phase does not compensate the Cu depletion towards the back contact within the chalcopyrite. Since, one could think that In would be displaced from the chalcopyrite structure to the In–Se phase. Consequently, the content of both In and Cu would decrease inside the chalcopyrite structure at the back interface, resulting in a stoichiometry at that interface different than the stoichiometry at the front interface. However, this would be not in agreement with the position of the A_1 Raman mode of CIGSe (see Supporting information, Figure S - 7) observed at the rear interface, which is the same as at the front interface for both ITO-MLU and ITO-IREC samples [71].

3.4. 2.5 × 2.5 cm^2 mini-module prototypes

After proving the chemical stability of the different ITO substrates during CIGSe growth, 2.5 × 2.5 cm^2 mini-modules with 3 cells were fabricated as described in the experimental section. Fig. 5 a) shows the visual appearance of the back contacts before (left) and after (right) solar cell fabrication with a maximum substrate temperature of 540 °C during CIGSe deposition. The transparency of the three different back contacts is weakly modified by CIGSe processing. ITO-MLU and ITO-IREC + Mo show a slightly increased transparency due to recrystallisation of ITO-MLU and selenisation of the functional Mo layer during CIGSe deposition, respectively. However, a reduced transparency can be observed for the bare ITO-IREC back contact, the darkening of which is due to the formation of In–Se phases, as indicated by Raman measurements (see above as well as Ref. [14]).

Highest efficiency is obtained for the mini-module with the ITO-IREC + Mo back contact, as shown in Fig. 5 a). Conversion efficiencies and currents in Fig. 5 are calculated by subtracting transparent and dead areas from the complete module area and normalizing the measured current to this solar active area.

The I–V curve of the bare ITO-IREC module is affected by a kink in the 1st quadrant and a reducing photocurrent with increasing forward voltage ($V < V_{OC}$), implying an injection and extraction barrier for majority carriers at the back contact. GDOES elemental depth profiles measured on a bare ITO-IREC reference device with identical I–V characteristics (see Supporting information Figure S - 8 a)) reveal the formation of GaO_x indicated by Ga segregation at the rear CIGSe/ITO interface. This is surprising, because for the devices shown in Fig. 5 we made use of a 70 nm In_2Se_3 precursor before co-evaporating Ga in the 1st stage of CIGSe processing. This precursor was thought to prevent GaO_x formation at the CIGSe/ITO interface. Additionally, a 5 nm KF precursor was applied in order to reduce the diffusion of Ga towards the ITO back contact. As a result, a strong Ga notch is present at a depth of ≈350 nm (see Supporting information Figure S - 8). However, J-V characteristics and parameters of simultaneously processed reference single cells with grid fingers on a standard Molybdenum back contact shown in the inset of Fig. 5 b) are close to our baseline devices.

The I–V characteristics of modules with a 300 nm ITO-MLU (hereafter designated as bare ITO-MLU) back contact show either a quasi-ohmic behaviour or a transport barrier for the diode current under forward bias. Despite reducing the nominal substrate temperature from 600 °C to 540 °C for module production, this behaviour is identical to the J-V characteristics of solar cells from the previous in-situ XRD experiments presented in Fig. 3 a). Accordingly, we find for two modules originating from the very same CIGSe and ITO-MLU back contact batch two different I–V performances. For one module we observe a regular I–V curve as shown in Fig. 5 b). The other module exhibits a kink in the 1st quadrant (not shown) and values of FF, V_{OC} and η, which are comparable to the bare ITO-IREC module with a similar kink shown in Fig. 5. Additionally, an accumulation of Ga signalling the formation of GaO_x at the rear interface has been detected in GDOES elemental depth profiles of the bare ITO-MLU back contact module with the distorted I–V curve (see Supporting information Figure S - 8b)). Whether GaO_x formed at the back contact of the bare ITO-MLU module with the regular I–V curve in Fig. 5 b), could not be verified due to narrow cell columns after the selective removal process (smaller than the sputter diameter of our GDOES system).

After demonstrating the functionality of semi-transparent 2.5 × 2.5 cm^2 mini-modules with CIGSe absorbers grown at substrate temperatures of up to 540 °C, we increased the substrate temperature to 625 °C. In case of bare ITO-MLU back contact modules, this led to I–V characteristics distorted by a kink in the 1st quadrant together with significant Ga accumulation at the rear interface visible in GDOES depth profiles. Consequently, V_{OC} of these mini-modules lies at around 1.7 V and FF does not exceed 40% (see Supporting information Figure S - 9).

Since such inferior I–V characteristics and GaO_x formation at the rear interface appeared for all bare ITO-IREC back contact mini-modules already at low substrate temperature of 540 °C, we did not include this back contact in the study with 625 °C substrate temperature during CIGSe growth.

However, in case of ITO-IREC + Mo mini-modules neither an enhancement nor a reduction of V_{OC} and FF upon increasing the substrate temperature from 540 °C to 625 °C was observed. Possibly, the improvement of CIGSe quality is not visible because of a module performance limitation by a high series resistance due to an undersized thickness of the front side TCO. This assumption is supported by the almost identical slope in the 1st quadrant of the I–V curves of the 300 nm ITO-MLU and the 800 nm ITO-IREC + Mo mini-modules in Fig. 5 b). Because, for single cells with metal grid, usually this slope and therewith the series resistance is limited by the conductivity of the back contact. Hence, single cells with ITO-MLU back contact have in general a reduced FF by 5% compared to cells with the higher conductive ITO-IREC + Mo back contact.

Finally we note, that at the elevated substrate temperature of 625 °C during CIGSe growth an increased transparency of the functional Mo layer becomes visible after selective removal of the cell stack (shown in Supporting information Figure S - 10) due to the higher selenization of the Mo. However the initial thickness (20 nm) of the Mo is not optimized to guarantee a complete selenization at this temperature, explaining the low transparency of the contacts in these samples. As reported in Ref. [14] decreasing the thickness of the deposited Mo FL to 10 nm allows full selenization of the Mo layer during the co-evaporation process without affecting the electrical quality of the back contacts, and this allows to increase the transparency of the back contact to AVT = 50%.

3.5. Upscaling: 10 × 10 cm^2 module prototypes

With the knowledge from manufacturing 2.5 × 2.5 cm^2 mini-modules, we transferred the developed process routines to our

maximum feasible substrate size of 10 × 10 cm^2. Now, only ITO-IREC + Mo served as transparent back contact. The nominal substrate temperature during CIGSe growth was 625 °C, which caused a slight plastic deformation of the modules after CIGSe processing. Due to an unfavourable negative gradient of the conduction band minimum towards the back contact within the CIGSe absorber, the ineffective application of an In_2Se_3 precursor was omitted. Dark and illuminated I–V characteristics measured under standard testing conditions (STC) are shown in the lower graph of Fig. 6. Curve (c) has been measured before equipping the module with a silver-grid by thermal evaporation through a shadow mask. The illuminated (a) and dark I–V curve (b) were obtained after front side metallization. Proportions and module dimensions can be seen in the upper images of Fig. 6. The transparent area after selective removal amounts to ≈30% of the solar active module area. In the magnified detail of Fig. 6 a large distance of 1.8 mm in between the P1 and the $P3_2$ scribes ($P3_1$ scribe before Ag grid) can be obtained. Together with the edges, the complete dead area amounts to 25% of the complete module area. Accordingly, the module efficiency is only ≈6% despite a FF of 63.6%. Taking into account the solar active area alone would give an idealized efficiency of ≈13%. Next to reducing the dead area further room for improvement is given by applying an anti-reflective coating and reducing the series resistance (R_S) of the module as indicated by the modest slope of the I–V curve (a) under forward bias in Fig. 6. We cannot conclude, whether the high R_S is dominated by the front or back contact and if V_{OC} (576 mV per cell) is affected by R_S in combination with localized shunts as it is maybe the case for curve (c). This has been confirmed by analyzing the equivalent circuit of a module with 4 sub-cells connected in series and each sub-cell represented by 5 cells connected in parallel (not shown here). Increasing V_{OC} after implementing a metal grid was observed in the case of adding a localized shunt within one of the sub-cells, leading to a similar transformation as curve (c)–(a), shown in Fig. 6. Since the grid forwards the photocurrent of non-shunted regions to the next sub-cell, which corresponds to a reduced current towards the local shunt, with the result that V_{OC} of the affected sub-cell and the complete module increases.

In contrast to the I–V characteristics of the 2.5 × 2.5 cm^2 mini-modules in Fig. 5 b), the upscaled 10 × 10 cm^2 mini-module shows a severe cross-over between illuminated and dark I–V curves. Such a cross-over in single solar cells can be attributed to an illumination dependent injection barrier for electrons at the front of the CIGSe absorber [72] or to an illumination dependent recombination rate of minority charge carriers within the depletion and/or quasi-neutral region of the absorber [73]. In case of our mini-module another reason could be the heating of the mini-module during illumination due to a poor thermal contact of the bended glass substrate to the cooling stage.

3.6. Long term outdoor testing of 10 × 10 cm^2 module prototype

For outdoor testing, the module shown in Fig. 6 has been encapsulated with a window glass on the front side of the module. As shown in Figure S - 11 the CIGSe semi-transparent module has been mounted via a plastic frame together with a Si-reference module with 40° inclination on the roof of IREC headquarters (Barcelona, Spain - 41° 24′ 56″ N, 2° 13′ 14″ E). Over highly stable resistors sized to match the MPP of the modules (R_{Si} = 66 Ω and R_{CIGSe} = 99 Ω), the output voltage V of the CIGSe and the Si reference has been monitored every 2 min without MPP tracking for more than 3 months. From the measurements the output power $P = V^2/R_i$ (i = Si, CIGSe) has been obtained.

With the help of the Si-reference module, the time dependent performance of the CIGSe module can be evaluated qualitatively. To distinguish between environmental illumination conditions and degradation of the CIGSe module, Fig. 7 shows the ratio $\varepsilon_{CIGSe,i}/\varepsilon_{Si,i}$, where $\varepsilon_{M,i} = E_{M,i}/E_{M,0}$ (M = CIGSe, Si) is the energy generation $E_{M,i} = \int P_{M,i}(t)dt$ per day normalized to the energy generation of the initial day i = 0 with i the consecutive number of days. In the ideal case without degradation, a linear fit of the normalized energy generation ratio should give a constant function with $y(x) \approx 1$.

However, in Fig. 7 we find initially up to day 40 a decreasing trend in energy generation of the CIGSe module compared to the Si-reference module. We attribute this to soiling of the front side glass

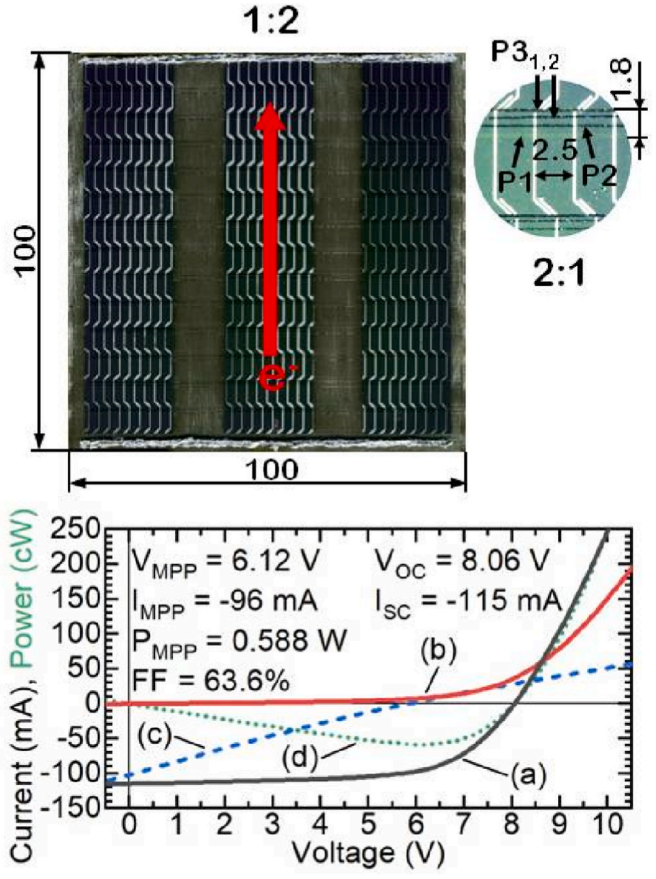

Fig. 6. Top view of 10 × 10 cm^2 semi-transparent mini-module with magnified view of the scribes and the metal grid. All dimensions are in millimetres. Bottom graph: Dark and illuminated I–V characteristics measured under STC with (a), (b) after and (c) before applying an Ag metal grid. (d) Output power as a function of voltage.

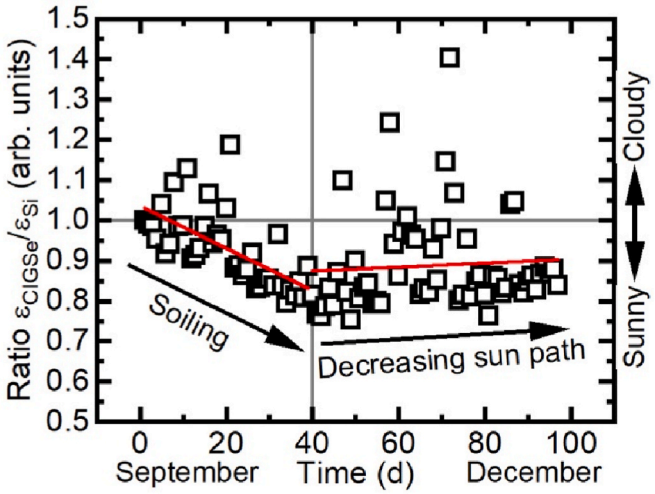

Fig. 7. Ratio of normalized energies generated per day plotted against the testing time under outdoor conditions. Red lines are obtained from linear data fitting within the specific range. (For interpretation of the references to colour in this figure legend, the reader is referred to the Web version of this article.)

encapsulating the CIGSe module shown in Figure S - 11 b). After day 40, the normalized energy generation ratio stabilizes and even shows a slight increasing trend with time. As indicated by the months on the bottom of Fig. 7, the outdoor test took place between September and December. Hence, the sun path lowered during the test period. Consequently, we expect that the slight increase of $\varepsilon_{CIGSe,i}/\varepsilon_{Si,i}$ is due to the well-known superior low light-intensity behaviour of CIGSe compared to Si modules [74]. A similar behaviour can be observed for cloudy days. The highest $\varepsilon_{CIGSe,i}/\varepsilon_{Si,i}$ ratio of ≈1.4 was obtained on day 70. On this day, the total amount of generated energy was less than 1% compared to the initial day 1 for both Si-reference and CIGSe module. In view of the constantly superior low light-intensity performance as well as the slightly increasing mean $\varepsilon_{CIGSe,i}/\varepsilon_{Si,i}$ ratio after day 40, we conclude that the initial performance loss of the CIGSe module is not due to module degradation but originates from soiling of the front side glass cover.

4. Conclusions

With in-situ XRD CIGSe growth experiments, we were able to show that bare ITO and ITO + Mo back contacts exhibit chemical stability at high temperatures (600 °C) in a selenium atmosphere. ITO back contacts without former annealing tend to re-crystallize during the substrates heating up before CIGSe processing. This kind of vacuum annealing affects the formation of an ITO bi-layer with a stress-free bottom-layer and an in-plane compressive strained top layer. ITO back contacts annealed in different atmospheres show no change in their XRD pattern throughout the complete CIGSe deposition process. Furthermore, we find that CIGSe layers grown on as fabricated ITO tend to have a preferred (112) texture. Annealing the Ar sputtered ITO back contacts in air or sputtering them by admixing oxygen changes the texture of deposited CIGSe layers in favour of a (220/204) orientation. No impact of air-annealing, admixing oxygen and ITO texture on GaO_x formation at the rear ITO/CIGSe interface has been observed. In contrast, increasing the ITO back contact thickness from 300 to 800 nm enhances GaO_x formation at the rear interface. Notwithstanding the formation of GaO_x at the rear interface, single solar cells with 300 nm thick ITO back contacts and CIGSe absorbers deposited at high substrate temperatures of 600 °C occasionally have quasi-ohmic J-V characteristics (FF > 70%), but also distorted J-V curves in other samples. Variations in Na supply or ITO surface roughness are debated reasons for this inconsistent behaviour. In case of 800 nm thick bare ITO back contacts, all of our devices have J-V characteristics affected by a transport barrier for the diode current in forward direction. By introducing a thin 20 nm Mo functional layer between the ITO back contact and CIGSe absorber the interfacial GaO_x vanishes together with the transport barrier. We conclude that GaO_x at the rear interface causes an injection/extraction barrier for holes in devices with a bare ITO back contact. Based on the 800 nm ITO +20 nm Mo back contact we built a 10 × 10 cm^2 semi-transparent mini-module with 14 sub cells, revealing the potential of 13% efficiency (active area). The theoretical optical transparency of this device amounts to ≈30%. However, due to the high opacity of the ITO + Mo back contact, the actual transparency integrated over the total module area is ≈ 10%. Improvement of module transparency could be achieved by changing the delamination technique from mechanical scribing to e. g. laser ablation and additionally removing the opaque back contact (see Ref. [9]). Further, ITO could be replaced by a TCO with higher transparency like In_2O_3:H (see Ref. [19]). Nevertheless, the back mirror effect of a Mo standard back contact can be avoided by the ITO + Mo back contact. Outdoor testing of the manufactured mini-module indicated mechanical and electrical stability over the complete testing period of 3 months. During this testing period, under low light illumination a superior performance of the ST CIGSe module compared to the Si reference-module has been observed. From these results we conclude the feasibility and high potential for applying semi-transparent CIGSe modules based on an ITO + Mo back contact in BIPV.

CRediT authorship contribution statement

Torsten Hölscher: Writing – review & editing, Writing – original draft, Methodology, Investigation, Formal analysis, Data curation, Conceptualization. **Marcel Placidi:** Writing – review & editing, Investigation, Formal analysis. **Ignacio Becerril-Romero:** Writing – review & editing, Methodology, Investigation, Formal analysis. **Robert Fonoll-Rubio:** Writing – review & editing, Methodology, Investigation, Formal analysis. **Victor Izquierdo-Roca:** Writing – review & editing, Methodology, Investigation, Formal analysis. **Angélica Thomere:** Writing – review & editing, Methodology, Investigation, Formal analysis. **Eduard Bailo:** Writing – review & editing, Methodology, Investigation, Formal analysis. **Thomas Schneider:** Methodology, Investigation, Formal analysis. **Heiko Kempa:** Writing – review & editing, Supervision. **Roland Scheer:** Writing – review & editing, Supervision, Project administration. **Alejandro Pérez-Rodríguez:** Writing – review & editing, Supervision, Project administration.

Declaration of competing interest

The authors declare that they have no known competing financial interests or personal relationships that could have appeared to influence the work reported in this paper.

Data availability

Data will be made available on request.

Acknowledgement

This work was part of the R + D + i Cell2Win project ref. PID 2019-104372RB-C31 funded by MCIN/AEI/10.13039/5011000110033 and the R + D + i i MasterPV project ref. PCI 2018–092945 funded by MCIN/AEI/10.13039/5011000110033 and cofunded by the European Union. Project MasterPV was supported under the umbrella of ERA.NET" title = "http://SOLAR-ERA.NET">SOLAR-ERA.NET and cofunded by “Agencia Estatal de Investigacion” (AEI,Spain), CDTI (Spain), and BMWi/PTJ (Germany, FKZ 0324230). ERA.NET" title = "http://SOLAR-ERA.NET">SOLAR-ERA.NET was supported by the European Commission within the EU Framework Programme for Research and Innovation HORIZON2020 (cofunded by ERA-NET Action, N691664). Authors from IREC belong to the Solar Energy Materials and Systems (SEMS) Consolidated Research Group of the “Generalitat de Catalunya” (ref.2017 SGR 862). M.P. acknowledges the financial support from Spanish Ministry of Science, Innovation and Universities within the Ramón y Cajal (RYC-2017–23758) program.

Appendix A. Supplementary data

Supplementary data to this article can be found online at https://doi.org/10.1016/j.solmat.2022.112169.

References

[1] U. Rau, A. Jasenek, R. Herberholz, H.-W. Schock, J.-F. Guillemoles, D. Lincot, L. Kronik, The inherent stability of Cu (In, Ga) Se2-based solar cells, in: Proc, 2nd WCPEC, 1998, pp. 428–433.
[2] R. Scheer, H.-W. Schock, Chalcogenide Photovoltaics: Physics, Technologies, and Thin Film Devices, John Wiley & Sons, 2011.
[3] M. Theelen, F. Daume, Stability of Cu (In, Ga) Se2 solar cells: a literature review, Sol. Energy 133 (2016) 586–627.
[4] M. Powalla, S. Paetel, D. Hariskos, R. Wuerz, F. Kessler, P. Lechner, W. Wischmann, T.M. Friedlmeier, Advances in cost-efficient thin-film photovoltaics based on Cu (In, Ga) Se2, Eng. Times 3 (4) (2017) 445–451.
[5] C.S.P. López, M. Sangiorgi, Comparison assessment of BIPV façade semi-transparent modules: further insights on human comfort conditions, Energy Proc. 48 (2014) 1419–1428.

[6] M.J. Shin, A. Lee, J.H. Park, A. Cho, S.K. Ahn, D. Shin, J. Gwak, J.H. Yun, J. Yoo, J.-S. Cho, Ultrathin Cu (In, Ga) Se2 transparent photovoltaics: an alternative to conventional solar energy-harvesting windows, Nano Energy 92 (2022), 106711.

[7] K. Kim, W.N. Shafarman, Alternative device structures for CIGS-based solar cells with semi-transparent absorbers, Nano Energy 30 (2016) 488–493.

[8] A. Duchatelet, K. Nguyen, P.-P. Grand, D. Lincot, M. Paire, Self-aligned growth of thin film Cu (In, Ga) Se2 solar cells on various micropatterns, Appl. Phys. Lett. 109 (25) (2016), 253901.

[9] A. Jeong, J.M. Choi, H.J. Lee, G.Y. Kim, J.K. Park, W.M. Kim, S. Kuk, Z. Wang, D. J. Hwang, H. Yu, Transparent back-junction control in Cu (In, Ga) Se2 absorber for high-efficiency, color-neutral, and semitransparent solar module, Prog. Photovoltaics Res. Appl. 30 (7) (2022) 713–725.

[10] O. Lundberg, M. Bodegård, J. Malmström, L. Stolt, Influence of the Cu (In, Ga) Se2 thickness and Ga grading on solar cell performance, Prog. Photovoltaics Res. Appl. 11 (2) (2003) 77–88.

[11] E. Jarzembowski, F. Syrowatka, K. Kaufmann, W. Fränzel, T. Hölscher, R. Scheer, The influence of sodium on the molybdenum/Cu (In, Ga) Se2 interface recombination velocity, determined by time resolved photoluminescence, Appl. Phys. Lett. 107 (5) (2015), 051601.

[12] M. Gloeckler, J.R. Sites, Potential of submicrometer thickness Cu (In, Ga) Se 2 solar cells, J. Appl. Phys. 98 (10) (2005), 103703.

[13] N. Naghavi, Z. Jehl, F. Erfurth, J.-F. Guillemoles, F. Donsanti, I. Gérard, P. Tran-Van, M. Bouttemy, A. Etcheberry, J.-L. Pelouard, Ultrathin Cu (In, Ga) Se 2 solar cells, 003642-003645, in: 2011 37th IEEE Photovoltaic Specialists Conference, 2011.

[14] R. Fonoll-Rubio, M. Placidi, T. Hoelscher, A. Thomere, Z.J. Li-Kao, M. Guc, V. Izquierdo-Roca, R. Scheer, A. Pérez-Rodríguez, Characterization of the Stability of Indium Tin Oxide and Functional Layers for Semitransparent Back-Contact Applications on Cu (In, Ga) Se2 Solar Cells, Solar RRL, 2022, 2101071.

[15] T. Nakada, Y. Hirabayashi, T. Tokado, D. Ohmori, T. Mise, Novel device structure for Cu (In, Ga) Se2 thin film solar cells using transparent conducting oxide back and front contacts, Sol. Energy 77 (6) (2004) 739–747.

[16] T. Schneider, C. Dethloff, T. Hölscher, H. Kempa, R. Scheer, Comparison of Mo and ITO back contacts in CIGSe solar cells: vanishing of the main capacitance step, Prog. Photovoltaics Res. Appl. 30 (2) (2022) 191–202.

[17] T. Schneider, J. Tröndle, B. Fuhrmann, F. Syrowatka, A. Sprafke, R. Scheer, Ultrathin CIGSe solar cells with integrated structured back reflector, Solar RRL 4 (10) (2020), 2000295.

[18] L. Gouillart, A. Cattoni, J. Goffard, F. Donsanti, G. Patriarche, M. Jubault, N. Naghavi, S. Collin, Development of reflective back contacts for high-efficiency ultrathin Cu (In, Ga) Se2 solar cells, Thin Solid Films 672 (2019) 1–6.

[19] J. Keller, L. Stolt, O. Donzel-Gargand, T. Kubart, M. Edoff, Wide-gap Chalcopyrite Solar Cells with Indium Oxide Based Transparent Back Contacts, Solar RRL, 2022.

[20] Y. Li, G. Yin, M. Schmid, Bifacial semi-transparent ultra-thin Cu (In, Ga) Se2 solar cells on ITO substrate: how ITO thickness and Na doping influence the performance, Sol. Energy Mater. Sol. Cell. 234 (2022), 111431.

[21] C. Wu, C. Wu, J. Sturm, A. Kahn, Surface modification of indium tin oxide by plasma treatment: an effective method to improve the efficiency, brightness, and reliability of organic light emitting devices, Appl. Phys. Lett. 70 (11) (1997) 1348–1350.

[22] N. Greenham, S. Moratti, D. Bradley, R. Friend, A. Holmes, Efficient light-emitting diodes based on polymers with high electron affinities, Nature 365 (6447) (1993) 628–630.

[23] T. Nakada, Y. Hirabayashi, T. Tokado, Cu (In1-x, Gax) Se2-based thin film solar cells using transparent conducting back contacts, 11A, L1209, Jpn. J. Appl. Phys. 41 (2002).

[24] S. Garud, N. Gampa, T.G. Allen, R. Kotipalli, D. Flandre, M. Batuk, J. Hadermann, M. Meuris, J. Poortmans, A. Smets, Surface passivation of CIGS solar cells using gallium oxide, Phys. Status Solidi 215 (7) (2018), 1700826.

[25] M. Heinemann, M. van Hest, M. Contreras, J. Perkins, A. Zakutayev, C. Kaufmann, T. Unold, D. Ginley, J. Berry, Amorphous oxides as electron transport layers in Cu (In, Ga) Se2 superstrate devices, Phys. Status Solidi 214 (5) (2017), 1600870.

[26] W. Witte, S. Paetel, R. Menner, A. Bauer, D. Hariskos, The application of sputtered gallium oxide as buffer for Cu (In, Ga) Se2 solar cells, Phys. Status Solidi Rapid Res. Lett. 15 (9) (2021), 2100180.

[27] T. Nakada, Microstructural and diffusion properties of CIGS thin film solar cells fabricated using transparent conducting oxide back contacts, Thin Solid Films 480 (2005) 419–425.

[28] Y. Li, G. Yin, Y. Gao, T. Köhler, J. Lucaßen, M. Schmid, Sodium control in Ultrathin Cu (In, Ga) Se2 solar cells on transparent back contact for efficiencies beyond 12, Sol. Energy Mater. Sol. Cell. 223 (2021), 110969.

[29] Y.-S. Son, H. Yu, J.-K. Park, W.M. Kim, S.-Y. Ahn, W. Choi, D. Kim, J.-h. Jeong, Control of structural and electrical properties of indium tin oxide (ITO)/Cu (In, Ga) Se2 interface for transparent back-contact applications, J. Phys. Chem. C 123 (3) (2019) 1635–1644.

[30] M. Saifullah, D. Kim, J.-S. Cho, S. Ahn, S. Ahn, J.H. Yun, H.S. Lee, J.H. Park, The role of NaF post-deposition treatment on the photovoltaic characteristics of semitransparent ultrathin Cu (In, Ga) Se 2 solar cells prepared on indium-tin-oxide back contacts: a comparative study, J. Mater. Chem. 7 (38) (2019) 21843–21853.

[31] P. Rostan, J. Mattheis, G. Bilger, U. Rau, J. Werner, Formation of transparent and ohmic ZnO: Al/MoSe2 contacts for bifacial Cu (In, Ga) Se2 solar cells and tandem structures, Thin Solid Films 480 (2005) 67–70.

[32] M. Saifullah, S. Ahn, J. Gwak, S. Ahn, K. Kim, J. Cho, J.H. Park, Y.J. Eo, A. Cho, J.-S. Yoo, Development of semitransparent CIGS thin-film solar cells modified with a sulfurized-AgGa layer for building applications, J. Mater. Chem. 4 (27) (2016) 10542–10551.

[33] A.M. Gabor, J.R. Tuttle, D.S. Albin, M.A. Contreras, R. Noufi, A.M. Hermann, High-efficiency CuIn x Ga1− x Se2 solar cells made from (In x, Ga1− x)2Se3 precursor films, Appl. Phys. Lett. 65 (2) (1994) 198–200.

[34] P. Pistor, S. Zahedi-Azad, S. Hartnauer, L.A. Wägele, E. Jarzembowski, R. Scheer, Real time observation of phase formations by XRD during Ga-rich or In-rich Cu (In, Ga) Se2 growth by co-evaporation, Phys. Status Solidi 212 (9) (2015) 1897–1904.

[35] G. Kaune, S. Hartnauer, R. Scheer, In situ XRD investigation of Cu2ZnSnSe4 thin film growth by thermal co-evaporation, Phys. Status Solidi 211 (9) (2014) 1991–1996.

[36] T.O. Mason, G. Gonzalez, J.-H. Hwang, D. Kammler, Point defects and related properties of highly co-doped bixbyite in 2 O 3, Phys. Chem. Chem. Phys. 5 (11) (2003) 2183–2189.

[37] D. Raoufi, A. Kiasatpour, H.R. Fallah, A.S.H. Rozatian, Surface characterization and microstructure of ITO thin films at different annealing temperatures, Appl. Surf. Sci. 253 (23) (2007) 9085–9090.

[38] G. Legeay, X. Castel, A gradual annealing of amorphous sputtered indium tin oxide: crystalline structure and electrical characteristics, Thin Solid Films 520 (11) (2012) 4021–4025.

[39] D. Mergel, M. Schenkel, M. Ghebre, M. Sulkowski, Structural and electrical properties of In2O3: Sn films prepared by radio-frequency sputtering, Thin Solid Films 392 (1) (2001) 91–97.

[40] N. Nadaud, N. Lequeux, M. Nanot, J. Jove, T. Roisnel, Structural studies of tin-doped indium oxide (ITO) and In4Sn3O12, J. Solid State Chem. 135 (1) (1998) 140–148.

[41] T. Minami, Y. Takeda, S. Takata, T. Kakumu, Preparation of transparent conducting In4Sn3O12 thin films by DC magnetron sputtering, Thin Solid Films 308 (1997) 13–18.

[42] G. González, T. Mason, J. Quintana, O. Warschkow, D.E. Ellis, J.-H. Hwang, J. P. Hodges, J. Jorgensen, Defect structure studies of bulk and nano-indium-tin oxide, J. Appl. Phys. 96 (7) (2004) 3912–3920.

[43] R. Keller, W. Holzapfel, H. Schulz, Effect of pressure on the atom positions in Se and Te, Phys. Rev. B 16 (10) (1977) 4404.

[44] Z. Cernosek, A. Růzicka, J. Holubova, E. Cernosková, An X-ray crystallographic study of new monoclinic selenium allotrope δ-Se8, Main Group Met. Chem. 30 (5) (2007) 231–234.

[45] M. Chong, K. Pita, S. Silalahi, Correlation between diffraction patterns and surface morphology to the model of oxygen diffusion into ITO films, Mater. Chem. Phys. 115 (1) (2009) 154–157.

[46] L. Bárdoš, M. Libra, Effect of the oxygen absorption on properties of ITO layers, Vacuum 39 (1) (1989) 33–36.

[47] L. Kerkache, A. Layadi, E. Dogheche, D. Remiens, Physical properties of RF sputtered ITO thin films and annealing effect, J. Phys. Appl. Phys. 39 (1) (2005) 184.

[48] D. Neerinck, T. Vink, Depth profiling of thin ITO films by grazing incidence X-ray diffraction, Thin Solid Films 278 (1–2) (1996) 12–17.

[49] J. Woolley, P. Keating, Solid solubility of In2Se3 in some compounds of zinc blende structure, J. Less Common Met. 3 (3) (1961) 194–201.

[50] Y.N.J. Ye, O. Nittono, Vacancy ordered structure of the III2VI3 compound semiconductor (GaxIn1− x) 2Se3 studied by electron diffraction and microscopy, Philos. Mag. A 73 (1) (1996) 169–186.

[51] M.A. Contreras, B. Egaas, D. King, A. Swartzlander, T. Dullweber, Texture manipulation of CuInSe2 thin films, Thin Solid Films 361 (2000) 167–171.

[52] M.A. Contreras, M.J. Romero, R. Noufi, Characterization of Cu (In, Ga) Se2 materials used in record performance solar cells, Thin Solid Films 511 (2006) 51–54.

[53] G. Hanna, T. Glatzel, S. Sadewasser, N. Ott, H. Strunk, U. Rau, J. Werner, Texture and electronic activity of grain boundaries in Cu (In, Ga) Se 2 thin films, Appl. Phys. A 82 (1) (2006) 1–7.

[54] S. Chaisitsak, A. Yamada, M. Konagai, Preferred orientation control of Cu (In1-xGax) Se2 (x≈ 0.28) thin films and its influence on solar cell characteristics, Jpn. J. Appl. Phys. 41 (2R) (2002) 507.

[55] S. Zahedi-Azad, E. Jarzembowski, S. Hartnauer, L. Wägele, D. Greiner, R. Scheer, Monitoring the phase evolution of Cu (In, Ga) Se2 by different Se flux via in-situ XRD, Phys. Status Solidi 213 (8) (2016) 2169–2175.

[56] C.V. Thompson, R. Carel, Texture development in polycrystalline thin films, Mater. Sci. Eng., B 32 (3) (1995) 211–219.

[57] J.-H. Yoon, K.-H. Yoon, J.-K. Kim, W.-m. Kim, J.-k. Park, T.S. Lee, Y.-J. Baik, T.-Y. Seong, J.-h. Jeong, Effect of the Mo back contact microstructure on the preferred orientation of CIGS thin films, 002443-002447, in: 35th IEEE Photovoltaic Specialists Conference, 2010, 2010.

[58] X. Dai, A. Zhou, L. Feng, Y. Wang, J. Xu, J. Li, Molybdenum thin films with low resistivity and superior adhesion deposited by radio-frequency magnetron sputtering at elevated temperature, Thin Solid Films 567 (2014) 64–71.

[59] T. Schlenker, V. Laptev, H. Schock, J. Werner, Substrate influence on cu (in, ga) se2 film texture, Thin Solid Films 480 (2005) 29–32.

[60] A. Hultqvist, P.M. Salomé, V. Fjällström, M. Edoff, B. Aitken, K. Zhang, Y. Shi, K. Fuller, C.K. Williams, Performance of Cu (In, Ga) Se2 solar cells using nominally alkali free glass substrates with varying coefficient of thermal expansion, J. Appl. Phys. 114 (9) (2013), 094501.

[61] M. Gloeckler, A. Fahrenbruch, J. Sites, Numerical modeling of CIGS and CdTe solar cells: setting the baseline, in 3rd World Conference onPhotovoltaic Energy Conversion, Proceedings (2003) 491–494, 2003.

[62] M. Burgelman, P. Nollet, S. Degrave, Modelling polycrystalline semiconductor solar cells, Thin Solid Films 361 (2000) 527–532.

[63] L. Pauw, A method of measuring specific resistivity and Hall effect of discs of arbitrary shape, Philips Res. Rep. 13 (1) (1958) 1–9.

[64] R. Scheer, L. Messmann-Vera, R. Klenk, H.W. Schock, On the role of non-doped ZnO in CIGSe solar cells, Prog. Photovoltaics Res. Appl. 20 (6) (2012) 619–624.
[65] C. Insignares-Cuello, C. Broussillou, V. Bermúdez, E. Saucedo, A. Pérez-Rodríguez, V. Izquierdo-Roca, Raman scattering analysis of electrodeposited Cu (In, Ga) Se2 solar cells: impact of ordered vacancy compounds on cell efficiency, Appl. Phys. Lett. 105 (2) (2014), 021905.
[66] J. Weszka, P. Daniel, A. Burian, A. Burian, A. Nguyen, Raman scattering in In2Se3 and InSe2 amorphous films, J. Non-Cryst. Solids 265 (1–2) (2000) 98–104.
[67] C.-H. Ho, Amorphous effect on the advancing of wide-range absorption and structural-phase transition in γ-In2Se3 polycrystalline layers, Sci. Rep. 4 (1) (2014) 1–8.
[68] I. Watanabe, T. Yamamoto, Electrical and structural properties of amorphous In-Se films prepared by flash evaporation, 10R, 1282, Jpn. J. Appl. Phys. 24 (1985).
[69] J. Weszka, P. Daniel, A. Burian, Raman spectra of In0. 30Se0. 70 amorphous films, Acta Physica Polonica-Series A General Physics 98 (5) (2000) 619–624.
[70] P. Pistor, R. Caballero, D. Hariskos, V. Izquierdo-Roca, R. Wächter, S. Schorr, R. Klenk, Quality and stability of compound indium sulphide as source material for buffer layers in Cu (In, Ga) Se2 solar cells, Sol. Energy Mater. Sol. Cell. 93 (1) (2009) 148–152.
[71] W. Witte, R. Kniese, M. Powalla, Raman investigations of Cu (In, Ga) Se2 thin films with various copper contents, Thin Solid Films 517 (2) (2008) 867–869.
[72] I. Eisgruber, J. Granata, J. Sites, J. Hou, J. Kessler, Blue-photon modification of nonstandard diode barrier in CuInSe2 solar cells, Sol. Energy Mater. Sol. Cell. 53 (3–4) (1998) 367–377.
[73] M. Nardone, S. Dahal, J. Waddle, Shading-induced failure in thin-film photovoltaic modules: electrothermal simulation with nonuniformities, Sol. Energy 139 (2016) 381–388.
[74] T. Feurer, P. Reinhard, E. Avancini, B. Bissig, J. Löckinger, P. Fuchs, R. Carron, T. P. Weiss, J. Perrenoud, S. Stutterheim, Progress in thin film CIGS photovoltaics–Research and development, manufacturing, and applications, Prog. Photovoltaics Res. Appl. 25 (7) (2017) 645–667.